Fast deterministic single-exposure coherent diffractive imaging at sub-Ångström resolution

A. J. Morgan,[1] A. J. D'Alfonso,[1] P. Wang,[2,3] H. Sawada,[4] A. I. Kirkland,[3] and L. J. Allen[1,*]

[1]*School of Physics, University of Melbourne, Parkville, Victoria 3010, Australia*

[2]*National Laboratory of Solid State Microstructures and Department of Materials Science and Engineering, Nanjing University, Nanjing 210093, People's Republic of China*

[3]*Department of Materials, University of Oxford, Parks Road, Oxford OX1 3PH, United Kingdom*

[4]*JEOL Ltd, 1-2 Musashino 3-Chome, Akishima, Tokyo 196, Japan*

(Received 7 August 2012; revised manuscript received 3 March 2013; published 27 March 2013)

In coherent diffractive imaging (CDI), conventional image-forming optics are replaced by the solution of an inverse scattering problem which obtains the exit surface wave from the diffraction pattern. To date CDI implementations typically use nonlinear iterative solutions, often using more than one diffraction pattern, and have been mainly implemented in the optical and x-ray regimes. Here we present single-exposure CDI reconstructions of a region of a cerium dioxide nanocrystal, illuminated by a coherent electron probe, in which the positions of both cerium and the lighter oxygen atoms are recovered simultaneously. We employ a fast deterministic algorithm based on the iterative solution of a set of linear equations with input data obtained from the inverse Fourier transform of the diffraction pattern. The solution of the linear equations proceeds using a conjugate gradient least-squares method based on fast Fourier transforms. This allows regularization of the inversion problem by iteration number, making it robust to experimental noise. This approach is successful where standard nonlinear phase retrieval techniques for the same data set are not.

DOI: 10.1103/PhysRevB.87.094115 PACS number(s): 42.30.Rx, 42.30.Wb, 61.05.jm, 61.05.jp

I. INTRODUCTION

Coherent diffractive imaging (CDI) dispenses with the use of lenses for imaging. CDI allows unaberrated representations of the specimen, in terms of both the amplitude and phase of the exit-surface wave, to be obtained, limited only by the wavelength of the incident radiation. The phase of the exit-surface wave is often the quantity of most interest from a structural and physical point of view. In x-ray imaging zone plates are often used as effective lenses[1] and their limitations have provided the impetus for the development of CDI by the x-ray community.[1,2] With advances in aberration correction for the lenses in modern electron microscopes,[3] the highest resolution achieved to date for images is around 0.05 nm,[4] about 25 times poorer than the diffraction limit for 300 keV electrons. Further improvement in lens performance will require an ever increasing effort for ever diminishing returns, an important reason for implementing CDI using electrons. In addition to resolution gains, electron CDI provides improved sensitivity to thin samples or light atoms.[5] The *raison d'etre* for electron CDI has also been discussed in a recent paper by Humphry *et al.*[6]

Humphry *et al.*[6] obtained the object transmission function for several gold nanoparticles using electrons, resolving atomic plane fringing with a spacing of 0.236 nm. Putkunz *et al.*[7] also recently demonstrated ptychographic imaging using a scanning transmission electron microscopy (STEM) probe to identify structure in a boron nitride helical cone at a resolution close to 0.1 nm. The success of ptychography derives from the overdetermination of the reconstruction of the transmission function by taking data at several (accurately determined or fitted) overlapping positions of the imaging probe. This overcomes the issues of sensitivity to noise and the ambiguities present in the usual nonlinear phase retrieval methods,[2,8] for which only a limited number of single-exposure results using electrons have been reported.[9–11] Ptychography also necessarily provides the specimen's transmission function over an extended region. We demonstrate an approach to CDI which is single-exposure (advantageous for radiation sensitive specimens, dynamic surfaces and systems, small nanoparticles, etc.), fast (allowing real-time imaging), deterministic, robust to the presence of noise, and which allows sub-Ångström resolution.

II. EXPERIMENT

Diffraction patterns of a cerium dioxide nanoparticle were obtained using the experimental setup in STEM shown schematically in Fig. 1(a). An atomic scale coherent electron probe is incident on the specimen to form a shadow image, also known as a Gabor hologram or Ronchigram. A JEOL R005 aberration corrected microscope with a cold field-emission gun (FEG)[12] operating at an accelerating voltage of 300 kV and with a probe-forming convergence semiangle of 24 mrad was used (implying an intrinsic resolution of 0.08 nm in real space).

The probe amplitude in the back focal plane was obtained from a bright-field image of the probe (a diffraction pattern taken without the presence of the sample which is effectively an image of the probe forming aperture). The phase related properties of the probe were obtained from the aberrations of the electron optical probe forming corrector measured using the microscope software. However, the nominal defocus of 91 nm was refined to 77 nm, as described in Sec. IV. Using this defocus value and the measured aberrations we computed the probe intensity at the specimen shown in Fig. 1(b).

Figure 1(c) shows a 1024 × 1024 pixel far-field diffraction pattern obtained by illuminating the edge of a cerium dioxide nanoparticle, cropped from the full field 2048 × 2048 pixel detector array. The larger array was used to obtain the wave in the exit surface plane of the nanoparticle. The image was recorded using a Gatan Ultrascan 1000 CCD camera with a nominal camera length of 12 cm and a pixel size at the detector plane of 16 μm. It should be noted that in the limit of a large

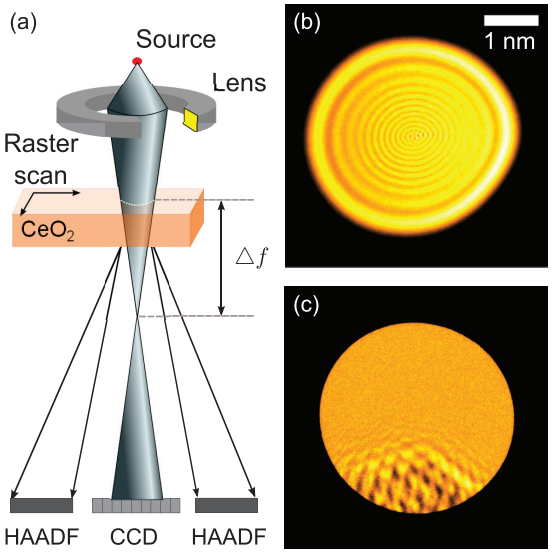

FIG. 1. (Color online) (a) Schematic representation of the STEM "shadow imaging" mode. (b) Intensity of the probe at a defocus of 77 nm (the exit surface plane). (c) Central portion (1024 × 1024 pixels) of the 2048 × 2048 pixel diffraction pattern.

probe forming aperture it can be shown that, in this imaging geometry, the diffraction pattern is a scaled representation of a defocussed image of the object.

III. THE EXIT SURFACE WAVE

A. Theoretical framework

We now discuss the recovery of the wave at the exit surface of the specimen from a diffraction pattern such as that shown in Fig. 1(c). One possible approach is to use one of the nonlinear iterative algorithms that can, in principle, be used to recover the exit surface wave.[2,8] Such approaches are multidimensional optimization procedures, very sensitive to measurement noise, and can stagnate in local minima in solution space. There is no formal method to ensure uniqueness of the solution.[2,8] We demonstrate a more robust deterministic approach which is widely applicable, with its genesis in the work of Martin and Allen and co-workers.[13–17] The wave at the exit surface of the specimen is written as a sum of the illumination $\psi_{\text{illum}}(\mathbf{r})$ and the modification thereof by the object $\psi_{\text{obj}}(\mathbf{r})$:

$$\psi_{\text{exit}}(\mathbf{r}) = \psi_{\text{illum}}(\mathbf{r}) + \psi_{\text{obj}}(\mathbf{r}), \tag{1}$$

where $\mathbf{r}$ is a vector in the exit surface plane of the object. For the reconstruction, the phase of the illumination incident on the nanocrystal was constructed in the back focal plane of the probe forming lens from the aberration coefficients, as discussed in Sec. II. The intensity of the probe in real space is shown in Fig. 1(b).

The inverse Fourier transform of the diffraction pattern, denoted $\mathcal{F}^{-1}[I(\mathbf{q})]$, is the autocorrelation of the exit surface wave. Using Eq. (1) we can write

$$\begin{aligned}\mathcal{F}^{-1}[I(\mathbf{q})] = {} & \psi_{\text{illum}}(\mathbf{r}) \otimes \psi_{\text{illum}}(\mathbf{r}) + \psi_{\text{obj}}(\mathbf{r}) \otimes \psi_{\text{obj}}(\mathbf{r}) \\ & + \psi_{\text{illum}}(\mathbf{r}) \otimes \psi_{\text{obj}}(\mathbf{r}) + \psi_{\text{obj}}(\mathbf{r}) \otimes \psi_{\text{illum}}(\mathbf{r}),\end{aligned} \tag{2}$$

where $\otimes$ represents the correlation operation. For example, $\psi_{\text{illum}}(\mathbf{r}) \otimes \psi_{\text{obj}}(\mathbf{r}) = \int \psi^*_{\text{illum}}(\mathbf{r}')\psi_{\text{obj}}(\mathbf{r}+\mathbf{r}')d\mathbf{r}'$. We assume

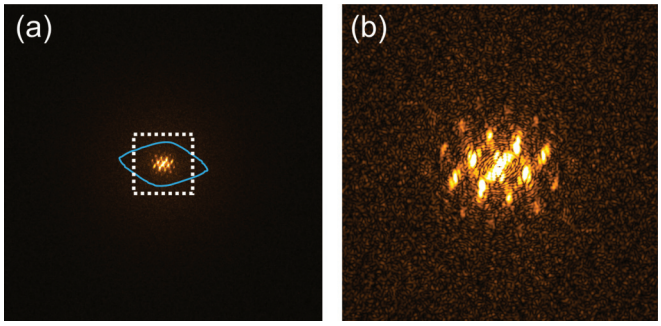

FIG. 2. (Color online) (a) Modulus of the inverse Fourier transform of the diffraction pattern in Fig. 1(c) after first subtracting the autocorrelation of the illumination. The roughly diamond shaped solid blue line is the area outside of which the autocorrelation of the object is assumed to be zero. (b) Detail of the area indicated by the dotted square outline in (a).

that the illumination is known so that the autocorrelation of the illumination, the first term on the right-hand side of Eq. (2), is also known and may be subtracted from the autocorrelation of the exit wave.

The inverse Fourier transform of the diffraction pattern shown in Fig. 1(c) minus the autocorrelation of the illumination is shown in Fig. 2(a). In Fig. 2(b) we show the detail of the area indicated by the dotted square outline in Fig. 2(a). The autocorrelation of the object, given by the second term in Eq. (2), is assumed to be zero outside the area indicated by the roughly diamond shaped blue solid line. The region of the illumination to which the object is confined, which determines the region outside of which the autocorrelation of the object is zero, is discussed later in the paper.

Note that in the two cross terms in the second line of Eq. (2) the unknown object function occurs linearly. If certain constraints on how the object is illuminated are fulfilled then there are sufficient linear equations in the autocorrelation (minus the autocorrelation of the illumination) inside the region where $\psi_{\text{obj}}(\mathbf{r}) \otimes \psi_{\text{obj}}(\mathbf{r})$ is assumed to be zero [Fig. 2(a) in this case] to solve unambiguously for $\psi_{\text{obj}}(\mathbf{r})$.[13] In contrast to previous work,[13–17] we assume here that the perturbation of the illumination by the object is small. In that case $\psi_{\text{obj}}(\mathbf{r}) \otimes \psi_{\text{obj}}(\mathbf{r})$ is a second order term and is neglected (at least initially since we can make a correction as described in the next subsection). This means that the cross terms over the whole autocorrelation plane are amenable to analysis in a linear fashion, not just those in the area where $\psi_{\text{obj}}(\mathbf{r}) \otimes \psi_{\text{obj}}(\mathbf{r})$ is strictly zero. This provides us with a vastly expanded data set to determine the same number of unknown exit wave values (defined by the area to which we believe that the object is confined). The expanded data set includes the structurally significant portion of the cross-correlation function [Fig. 2(b)]. This leads to a substantially more overdetermined inverse problem which is more robust to noise, a factor crucial to the results presented in this paper.

B. The linear equations

We briefly describe the setting up of the linear equations we solve to obtain $\psi_{\text{obj}}(\mathbf{r})$ in Eq. (1). We begin by writing the correlations on the second line of Eq. (2) (the cross terms) in

the form of discrete sums as

$$f_n^{\text{cross}} = \sum_m \psi_{n+m}^{\text{illum}} \psi_m^{*\text{obj}} + \sum_m \psi_m^{\text{obj}} \psi_{m-n}^{*\text{illum}}. \quad (3)$$

The labels "illum" and "obj" in Eq. (2) have been moved to be superscripts to facilitate the discrete notation.

Separating this into real and imaginary components, denoted by the superscripts (r) and (i) respectively, we obtain

$$\begin{aligned} & f_n^{\text{cross}(r)} + i f_n^{\text{cross}(i)} \\ &= \sum_m \left(\psi_{n+m}^{\text{illum}(r)} + i\psi_{n+m}^{\text{illum}(i)}\right)\left(\psi_m^{\text{obj}(r)} - i\psi_m^{\text{obj}(i)}\right) \\ &\quad + \sum_m \left(\psi_{m-n}^{\text{illum}(r)} - i\psi_{m-n}^{\text{illum}(i)}\right)\left(\psi_m^{\text{obj}(r)} + i\psi_m^{\text{obj}(i)}\right). \end{aligned} \quad (4)$$

Writing this in matrix form we have

$$\begin{bmatrix} \sum_m \left(\psi_{n+m}^{\text{illum}(r)} + \psi_{m-n}^{\text{illum}(r)}\right) & \sum_m \left(\psi_{n+m}^{\text{illum}(i)} + \psi_{m-n}^{\text{illum}(i)}\right) \\ \sum_m \left(\psi_{n+m}^{\text{illum}(i)} - \psi_{m-n}^{\text{illum}(i)}\right) & \sum_m \left(-\psi_{n+m}^{\text{illum}(r)} + \psi_{m-n}^{\text{illum}(r)}\right) \end{bmatrix} \times \begin{bmatrix} \psi_m^{\text{obj}(r)} \\ \psi_m^{\text{obj}(i)} \end{bmatrix} = \begin{bmatrix} f_n^{\text{cross}(r)} \\ f_n^{\text{cross}(i)} \end{bmatrix}. \quad (5)$$

This is the set of linear equations which we now solve.

C. Implementation of the linear inversion process

We use the conjugate gradient least squares (CGLS) method to solve the system of linear equations[17] and extend our previous work by introducing regularization by iteration number, a crucial new component in the success of the method. Due to the particular structure of the coefficient matrix in this particular problem, the CGLS method can be cast in the form of a memory efficient algorithm based on Fourier transforms, dubbed iterative linear retrieval using Fourier transforms (ILRUFT).[17] The CGLS method coupled with regularization by iteration number is more robust to noise than solving the linear system by singular value decomposition (SVD) and then truncating the insignificant singular values. The CGLS method operates in a Krylov subspace that is defined in terms of both the coefficient matrix and the right-hand side of the linear equations, while the SVD approach depends solely on the coefficient matrix.[18] The Krylov subspace is adapted in an optimal way to the specific right-hand side, while the SVD basis is only optimal if no information about the right-hand side is utilized.[18] Thus the CGLS approach picks up the physical components of the solution first and spurious information, mostly attributed to noise, is excluded by a judicious truncation of the iterations. In a model problem, including simulations of noise, the residual [a measure of how well the right-hand side of Eq. (5) is reproduced] decreases monotonically with iteration number. However, after a certain number of iterations the fidelity of the solution (i.e., how far away the current solution of the set of linear equations is from the true object and which can be explicitly monitored in a model problem) stops improving and begins to deteriorate. This is because basis vectors in the Krylov subspace that are corrupted by noise start contributing to the solution.

Using an approach based on CGLS makes a single-exposure retrieval possible but considerably more problematic if the standard nonlinear approaches to phase retrieval are employed, where every step in the process is affected by noise. Further improvement can be obtained by estimating $\psi_{\text{obj}}(\mathbf{r}) \otimes \psi_{\text{obj}}(\mathbf{r})$ from our solution, subtracting this from the autocorrelation (already having subtracted the autocorrelation of the illumination) and repeating the linear solution. Even when the nonlinear term is significant numerical tests that we have carried out have shown this approach to be successful.

The area to which the object is assumed to be confined, or in other words the region for which we obtain a solution, was defined by the overlap between the edge of the nanoparticle and the spatial extent of the illumination in the sample plane. The spatial extent of the probe was assumed to be limited to 0.05 of the maximum value of the probe amplitude. The edge of the nanoparticle can be approximately identified by approximating the phase in the diffraction plane as that of the illumination (the amplitude being the square root of the measured diffraction pattern) and propagating to the exit surface plane. We note that a tight object support[19] is not necessary for the success of the retrieval, thus allowing some latitude with respect to a knowledge of the probe position. Figure 3(a) shows how the retrieval, treating the whole autocorrelation plane as being linearly related to $\psi_{\text{obj}}(\mathbf{r})$, proceeds by viewing the phase of the transmission function of the object. The first iteration already yields a good result. It is judged that the best result is obtained after three iterations. Thereafter ill-determined basis vectors start to pollute the solution, as can be seen by the noisier result obtained after seven iterations. We note that more noise is evident in all of the solutions at the bottom edge of the object support where the illumination is weaker. After 100 iterations the result is so corrupted that it bears no resemblance to the structure, which can be confirmed by taking a high-angle annular dark-field (HAADF) image of the specimen, as we will discuss in the next section and which is shown in Fig. 4(a). Using the result at the third iteration we estimate $\psi_{\text{obj}}(\mathbf{r}) \otimes \psi_{\text{obj}}(\mathbf{r})$ and subtract this (and the autocorrelation of the illumination) from the autocorrelation in Eq. (2). Having made this correction we then repeat our inversion. This gives the results shown in Fig. 3(b). Once again, regularizing by iteration number was used and termination occurred after three iterations and this result has a reduced residual, indicating an improved solution.

D. Comparison with nonlinear iterative methods

We next compare the behavior of two nonlinear iterative CDI algorithms to that of ILRUFT. We use the error reduction algorithm (ERA) and the hybrid input-output (HIO) method with a feedback parameter $\beta = 1$.[2,8,20,21] In each case we seed the nonlinear retrieval with the result obtained after three ILRUFT iterations (post nonlinear correction), shown in Fig. 3(b). In Fig. 3(c) we see that for increasing iteration number the ERA method moves away from this result rapidly as it is compromised by measurement noise in subsequent iterations. The same happens in the case of HIO, as can be seen in Fig. 3(d). Seeding either the ERA or HIO methods with a large number of other random starting points did not yield any solution approaching the quality of that obtained using the linear inversion procedure.

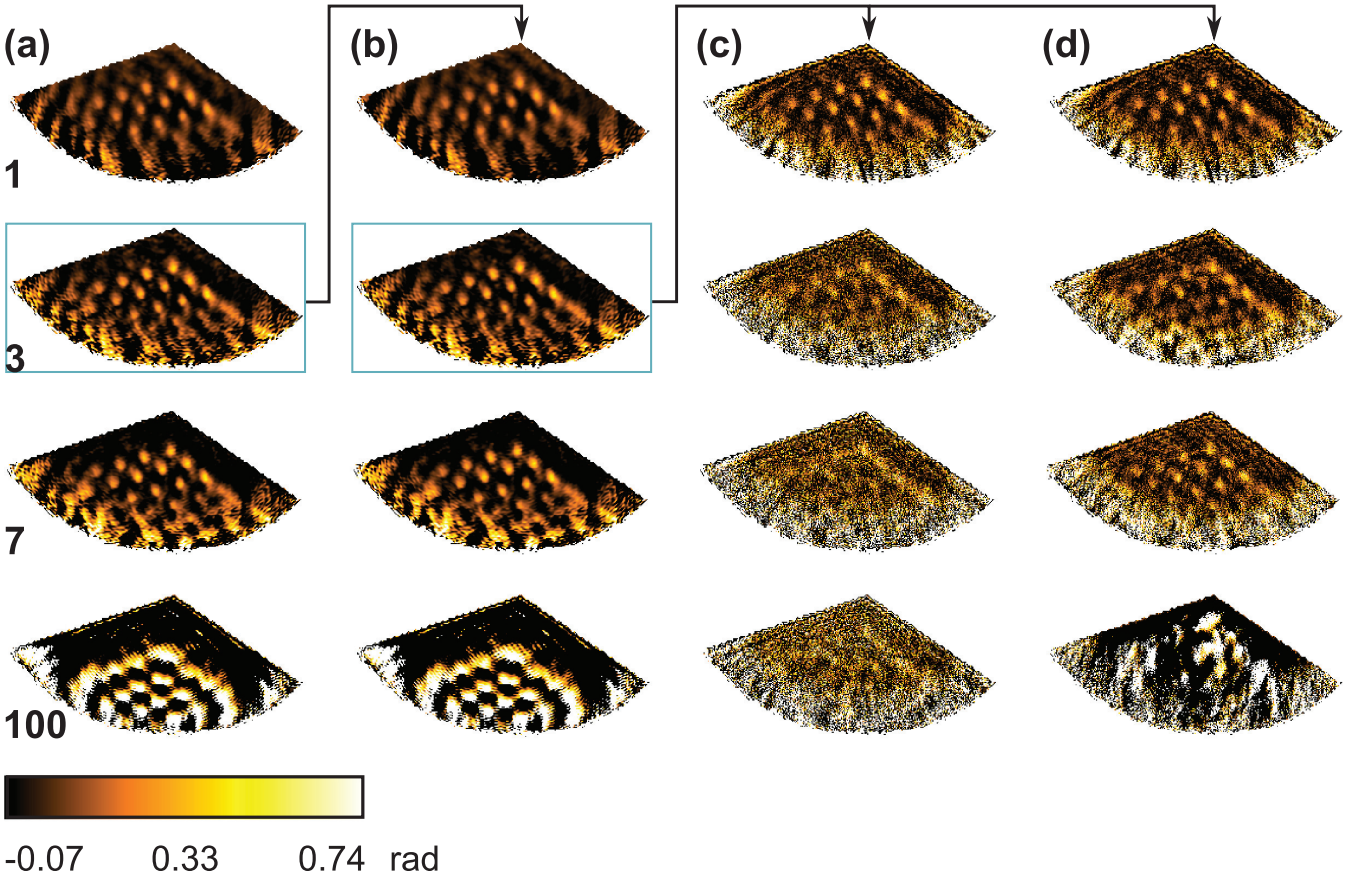

FIG. 3. (Color online) (a) Phase of the transmission function of the object obtained from the diffraction pattern shown in Fig. 1(c) after 1, 3, 7, and 100 iterations of ILRUFT. (b) Result obtained after correcting the autocorrelation for the nonlinear autocorrelation of the object obtained in (a) after three iterations. (c) Result of using the ERA, seeded with the result in (b) after three iterations. (d) Similar results for the HIO approach.

IV. VALIDATION OF THE APPROACH

The structure of the nanoparticle can also be explored by taking a HAADF image. This is shown in Fig. 4(a). Atoms contribute to the image contrast as the square of their atomic number Z (hence this mode of imaging is also known as Z-contrast imaging). Therefore columns of heavier cerium atoms can be seen but not the lighter oxygen atoms. The phase image shown in Fig. 3(b) (the exit surface wave divided by the illumination function describing the probe, i.e. the transmission function) after three ILRUFT iterations (post nonlinear correction) is shown in position relative to the HAADF image in Fig. 4(b), and a portion excised from it is overlaid on the HAADF image in Fig. 4(d).

The nominal defocus value of 91 nm (underfocus) estimated from the microscope software was refined during the reconstruction procedure using the fact that the dominant effect of defocus on the object reconstruction was to scale the interatomic distances between the columns of atoms in the retrieved phase images [such as that shown in Fig. 4(b)]. Defocus was adjusted until the interatomic distances were in register with the HAADF image in Fig. 4(a), yielding a refined defocus of 77 nm.

In Fig. 4(c) we show the phase image obtained independently for a second probe position, as indicated, which slightly overlaps the first probe position. This solution was obtained in the same fashion as that in the first position [Fig. 4(b)]. This is also overlaid, suitably cropped (and with no overlap with the first phase image), on the HAADF image in Fig. 4(d). We note that in the region of overlap the images are in fact consistent with each other.

We note that atomic columns with a few atoms near the edge of the specimen are resolved in the recovered phase, but this is not the case for the HAADF image. We suggest that observation of this unstable edge is facilitated by single-exposure imaging. Even more remarkably, columns of oxygen atoms between the cerium atoms are evident in the recovered phase but are not visible in the HAADF images, as we will now discuss.

From the structural information we have obtained from the specimen, we surmise that the structure is as shown in Fig. 5(a). In Fig. 5(b) we show a simulation of the diffraction pattern in Fig. 1(c), which is repeated in Fig. 5(c) for ease of comparison. The simulation takes into account the imaging conditions [the same probe as shown in Fig. 1(b)], temporal incoherence corresponding to an energy spread in the source of 0.5 eV,[12] an effective source size with FWHM 0.07 nm,[12] and the assumption that the particle adopts the energetically stable cubeoctahedral morphology.[22] The CDI reconstruction

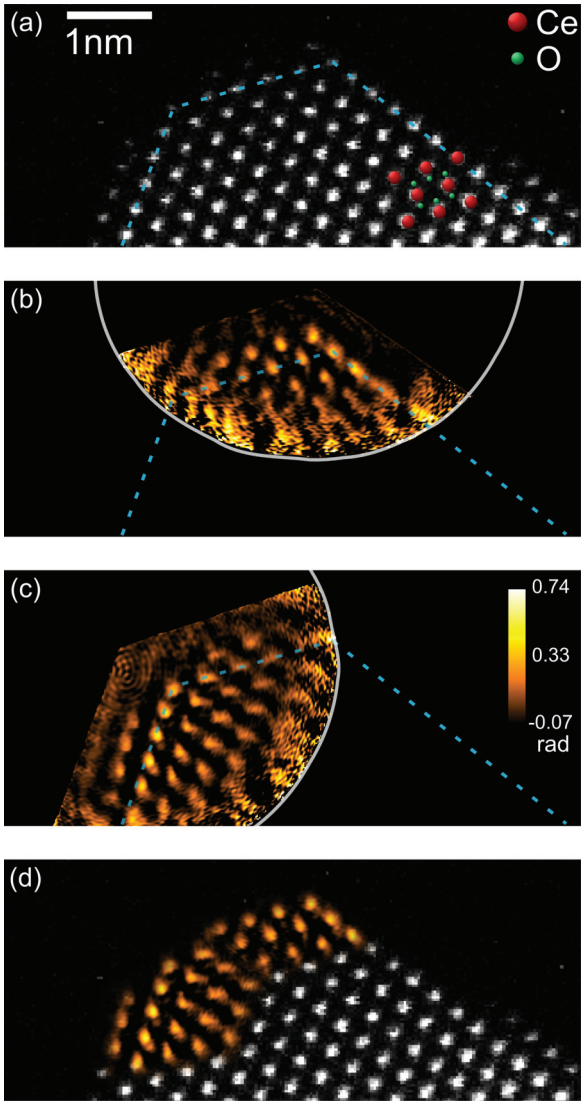

FIG. 4. (Color online) (a) HAADF image of the nanoparticle. (b) The phase image shown in Fig. 3(b) (the exit surface wave divided by the illumination function describing the probe, i.e. the transmission function) after three ILRUFT iterations post nonlinear correction is shown in position relative to the HAADF image in Fig. 4(a). (c) Phase image obtained independently for a second probe position, as indicated, which slightly overlaps the first probe position. (d) Suitably cropped portions of the phase images in (b) and (c) overlaid on the HAADF image in (a).

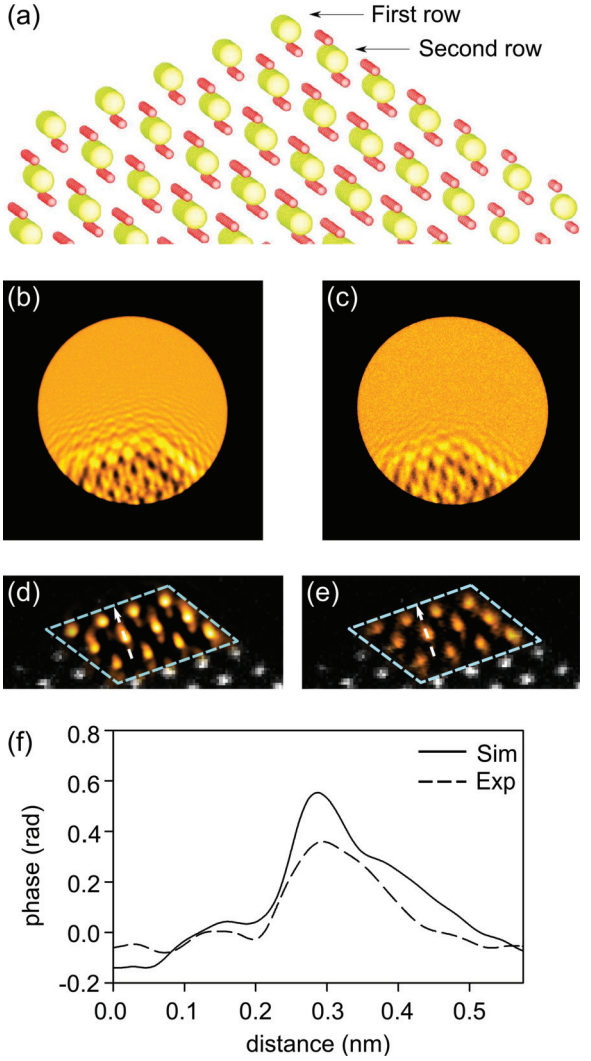

FIG. 5. (Color online) (a) Model structure of the edge of the CeO_2 nanoparticle (the indicated rows are cerium atoms). Simulation of the diffraction pattern in Fig. 1(c) [reproduced here in panel (c) for ease of comparison] is shown in (b). The CDI reconstruction obtained from the simulated result in (b) is shown inside the dashed outline and overlayed on the experimental Z-contrast image in (d). This can be compared with the experimental result shown in (e). Line scan over oxygen and cerium atom positions, as indicated in (d) and (e), and labeled Sim and Exp, respectively, are compared in (f).

obtained from the simulated diffraction pattern is shown in Fig. 5(d) and once again, for comparison purposes, the overlay in Fig. 4(d), for the probe position indicated in Fig. 4(b) is repeated in Fig. 5(e). Line scans over oxygen and cerium atom positions, as indicated in Figs. 5(d) and 5(e), are compared in Fig. 5(f). It should be noted that between 0.1 and 0.2 nm, where there is a column of oxygen atoms, both theory and experiment indicate this and are in close agreement. The column of oxygen atoms on the other side of the cerium column is not clearly evident in either the result obtained from experiment or the simulation, due to the morphology of the specimen and how the beam interacts with it.

V. SUMMARY AND CONCLUSION

We have demonstrated a fast deterministic approach to CDI, based on the iterative solution of sets of linear equations. By suitably truncating the number of iterations, the fitting of ill-determined components can be avoided, a control not afforded by the usual nonlinear CDI algorithms. This has allowed single-exposure retrievals of the transmission function of a cerium dioxide nanoparticle in which both cerium and the lighter oxygen atoms were observed simultaneously. A detailed simulation of the experiment, including the retrieval step, yielded a phase change due to transmission through the specimen in close agreement with that observed. In this method there is no restriction on the size or position of the object, provided it is illuminated by the beam. The extent in Fourier

space of the illumination is the primary determiner of the resolution.

ACKNOWLEDGMENTS

This research was supported under the Australian Research Council's Discovery Projects funding scheme (Project No. DP1096025) and its DECRA funding scheme (Project No. DE130100739) and by the EPSRC (Grant Nos. EP/E034055/1 and EP/F048009/1). The microscope was developed under the CREST R005 project, supported by the Japan Science and Technology Agency (Project leader: Kunio Takayanagi). A.J.M. acknowledges financial assistance by the David Hay Memorial Fund.

*lja@unimelb.edu.au

[1] K. A. Nugent, Adv. Phys. **59**, 1 (2010).
[2] H. M. Quiney, J. Mod. Opt. **57**, 1109 (2010).
[3] P. W. Hawkes, Phil. Trans. R. Soc. London, Ser. A **367**, 3637 (2009).
[4] R. Erni, M. D. Rossell, C. Kisielowski, and U. Dahmen, Phys. Rev. Lett. **102**, 096101 (2009).
[5] L. De Caro, E. Carlino, G. Caputo, P. D. Cozzoli, and C. Giannini, Nat. Nano **5**, 360 (2010).
[6] M. J. Humphry, B. Kraus, A. Hurst, A. M. Maiden, and J. M. Rodenburg, Nat.Comm. **3**, 730 (2012).
[7] C. T. Putkunz, A. J. D'Alfonso, A. J. Morgan, M. Weyland, C. Dwyer, L. Bourgeois, J. Etheridge, A. Roberts, R. E. Scholten, K. A. Nugent, and L. J. Allen, Phys. Rev. Lett. **108**, 073901 (2012).
[8] S. Marchesini, Rev. Sci. Instrum. **78**, 011301 (2007).
[9] J. M. Zuo, I. Vartanyants, M. Gao, R. Zhang, and L. A. Nagahara, Science **300**, 1419 (2003).
[10] O. Kamimura, K. Kawahara, T. Doi, T. Dobashi, T. Abe, and K. Gohara, Appl. Phys. Lett. **92**, 024106 (2008).
[11] R. Dronyak, K. S. Liang, Y. P. Stetsko, T.-K. Lee, C.-K. Feng, J.-S. Tsai, and F.-R. Chen, Appl. Phys. Lett. **95**, 111908 (2009).
[12] S. Kim, Y. Oshima, H. Sawada, T. Kaneyama, Y. Kondo, M. Takeguchi, Y. Nakayama, Y. Tanishiro, and K. Takayanagi, J. Elec. Microsc. **60**, 109 (2011).
[13] A. V. Martin and L. J. Allen, Opt. Commun. **281**, 5114 (2008).
[14] A. V. Martin, A. I. Bishop, D. M. Paganin, and L. J. Allen, Ultramicroscopy **111**, 777 (2011).
[15] A. J. Morgan, A. J. D'Alfonso, A. V. Martin, A. I. Bishop, H. M. Quiney, and L. J. Allen, Phys. Rev. B **84**, 144122 (2011).
[16] A. J. Morgan, A. V. Martin, A. J. D'Alfonso, C. T. Putkunz, and L. J. Allen, Ultramicroscopy **111**, 1455 (2011).
[17] A. J. D'Alfonso, A. J. Morgan, A. V. Martin, H. M. Quiney, and L. J. Allen, Phys. Rev. A **85**, 013816 (2012).
[18] P. C. Hansen, *Discrete Inverse Problems: Insight and Algorithms* (SIAM, Philadelphia, 2010).
[19] S. Marchesini, H. He, H. N. Chapman, S. P. Hau-Riege, A. Noy, M. R. Howells, U. Weierstall, and J. C. H. Spence, Phys. Rev. B **68**, 140101(R) (2003).
[20] R. W. Gerchberg and W. O. Saxton, Optik **35**, 237 (1972).
[21] J. Fienup, Appl. Opt. **21**, 2758 (1982).
[22] A. S. Barnard and A. I. Kirkland, Chem. Mat. **20**, 5460 (2008).